Strike-slip kinematics from crustal to outcrop-scale: the impact of the material properties on the analogue modelling

Luigi Massaro[1*], Jürgen Adam[2], Elham Jonade[2], Silvia Negrão[2], and Yasuhiro Yamada[2,3]

[1] Department of Civil, Architectural and Environmental Engineering, Università degli Studi di Napoli Federico II, Piazzale Tecchio, 80, Napoli, Italy,

[2] Department of Earth Sciences, Royal Holloway University of London, Egham, Surrey, TW20 0EX, United Kingdom

[3] Department of Earth Resources Engineering, Kyushu University, Fukuoka, 819-0395, Japan

*Corresponding author: luigi.massaro@unina.it

Abstract

Strike-slip fault zones commonly display complex kinematics and 3D geometries, with high structural variability along strike and with depth. In this regard, analogue modelling techniques represent a powerful tool for investigating the structural, kinematic and mechanical deformation processes at various scales. In detail, dynamically scaled experiments allow the direct comparison between model and natural systems. The geometric scaling factor defines the model resolution, in terms of model/prototype length equivalence, and depends on the mechanical and physical properties of the prototype and analogue materials.

In this paper, systematic strike-slip experiments were performed by applying four different model materials to investigate the deformation dynamics at various scales and to highlight the impact of the physical and mechanical properties of the model material on the experiments. The applied model materials showed a non-linear strain-dependent deformation behaviour while providing different dynamically scaled geometric scaling factors.

Digital Image Correlation (DIC) analyses of the experiments allowed a quantitative comparison of the displacement and strain fields at different stages of the dextral displacement above a single planar basement fault. The analysis of the localisation and development of the fractures in the strike-slip shear zones enabled the comparison of the different structural styles and dynamics observable at various levels of resolution. Therefore, the application of such a multi-scale approach in dynamically scaled experiments can provide new insights into the investigation of complex deformation processes with analogue modelling techniques.

Keywords: *Strike-slip kinematics; Rock fracture mechanics; Fault damage zone; Analogue modelling; Mechanical testing*

1. Introduction

Strike-slip fault zones are characterised by complex 3-D structures, with rapid changes in deformation along strike and with
30   depth (Wu et al., 2009). The development of the strike-slip faults initiates from arrays of *en echelon* fractures. With
increasing deformation, these early fractures further develop and link together, forming a continuous and complex strike-slip
shear zone (Crider and Peacock, 2004; Shipton and Cowie, 2001). The spatial properties of the damage and fault zones, as
well as the fracture network they develop, have a critical impact on the permeability and stability of rock masses, with direct
applications in resources management, e.g., water reservoir, geothermal energy (Massaro et al., 2019; Bisdom et al., 2014;
35   Zeng and Yao, 2016), risk mitigation, e.g., rockfalls (Schilirò et al., 2024; Mammoliti et al., 2023; Lambert et al., 2012), and
civil engineering constructions, e.g., tunnels (Wang et al., 2020; Cacciari and Futai, 2017).

Analogue modelling techniques allow the simulation of geological processes and the investigation of their evolution through
space and time. Dynamically scaled models enable the direct comparison between the experiment and the prototype. The
observations in the final model are, therefore, quantitative and not only qualitative. In this context, the model materials
40   applied in the experiment play a critical role in defining the scaling relationships. In fact, the dynamically scaled length
equivalence between the model and natural systems depends on the physical and mechanical properties of the model
materials applied and the rock prototype simulated. Therefore, the choice of the model materials strictly depends on the
processes and structures aimed to simulate.

In this study, we performed systematic strike-slip experiments with four analogue materials that enabled different levels of
45   dynamic scaling. The multi-scale comparison between the models highlighted the various insights that can be derived by
changing the scale of observation and the resolution of the model.

The strike-slip experiment, also referred to as 'Riedel experiment', consists of deforming an overburden above a single
planar and vertical basement fault with pure strike-slip movement (Dooley and Schreurs, 2012). The materials applied are
quartz sand, clay and GRAM (Massaro et al., 2022). The quartz sand was applied as 'dry' quartz sand and 'wet' quartz sand.
50   In the latter case, 10 wt% of water was added during the sample preparation. The clay was used in a mixture of quartz sand
with 5 wt% of clay. GRAM is a cohesive granular material composed of quartz sand, hemihydrate powder and water. In this
study, GRAM was used with 2 wt% of hemihydrate.

The physical and mechanical properties of the model materials were analysed, comparing their deformation behaviour under
different loading conditions. Also, their shear and frictional properties were determined. The mechanical properties are
55   necessary, along with the density, for the dynamic scaling calculation. The latter was defined by referring to a common
prototype (a generic sedimentary rock with 26.3 MPa of cohesion and a density of 2.37 g cm^{-3}, Kulhawy (1975). Dry sand
and sand-clay mixture enabled the simulation at the field scale, with 1 cm in the model corresponding to 927 and 637 m,
respectively. The geometric scaling factors calculated for the wet sand and GRAM 2% were 1 cm in the model
corresponding to 114 and 22 m, respectively.

60 The four models were compared from the top-view images analysed with strain-monitoring Digital Image Correlation (DIC) techniques. The investigation from the larger to the smaller scale represented a zoom-in into the fault systems, with the shear zone architecture showing increasing complexity. Thus, a multi-scale approach with analogue modelling techniques can provide fundamental insights into the analysis of complex brittle deformation processes.

2. Geological background

2.1 Strike-slip fault systems

65 Strike-slip fault systems commonly display complex geometries with high variability in depth and along strike. A fault system is a complex volume of deformed rock, composed of differently strained zones that present characteristic structures. The most internal part is the fault core, surrounded by the enveloping damage zones and, most externally, the undeformed host rock (Faulkner et al., 2010; Wibberley et al., 2008; Childs et al., 1996). Most of the displacement is accommodated by

70 the central fault core, resulting in intensely deformed rocks characterised by high-strain features, including cataclasite and ultra-cataclasite, breccia and clay-rich gouge zones. The surrounding damage zones undergo lower deformation, resulting in lower-strain deformation structures. These include a fracture network, secondary faults, veins, cleavage, folds, and deformation bends. The intensity of deformation of fault core and damage zones affects the permeability of the rock, which critically increases towards the outer part of the fault system (Billi et al., 2003; Choi et al., 2016; Faulkner et al., 2010; Kim

75 et al., 2004). Finally, the lateral reduction in strain leads to the transition from the damage zones to the undeformed host rock, which is not affected by the fault deformation.

2.1.1 Analogue modelling of strike-slip faults systems

Analogue modelling techniques have been applied by several studies to investigate strike-slip tectonics and individual aspects, including transtension, transpression, block rotation, fault zone segmentation, and strain partitioning. In general, the

80 model materials applied depend on the aims of the study as summarised in Table 1.

Table 1.

2.2 Analogue Modelling Scaling

The scaling theory represented a turning point for analogue modelling, upgrading it from a qualitative to a quantitative investigation method (Hubbert, 1937). A scaled model enables the direct comparison between the model and the natural

85 system. The scaling is composed of three hierarchical levels of similarity between the experiment and the rock prototype. The geometric scaling is the lowest of the three levels and requires that all the corresponding lengths (l_n, $n = 1, 2, 3, …$) are proportional and all the corresponding angles (α) are equal in the two systems, so that:

Eq. 1

$$\frac{l_1^m}{l_1^p} = \frac{l_2^m}{l_2^p} = \frac{l_3^m}{l_3^p} = \frac{l_n^m}{l_n^p} \quad \text{and} \quad \alpha_n^m = \alpha_n^p$$

90 Where m indicates the model and p the prototype.

The kinematic scaling involves the time required for the deformation to happen in the two systems, and must be scaled as follows (Ramberg, 1967):

Eq. 2

$$\frac{t_1^m}{t_1^p} = \frac{t_2^m}{t_2^p} = \frac{t_3^m}{t_3^p} = \frac{t_n^m}{t_n^p}$$

95 To obtain the highest level of similarity, i.e., the dynamic scaling, the angle of internal friction of the model material must be similar to the upper crustal rocks, 27°-45° (Handin, 1966; Jaeger et al., 2007). In addition, the physical and mechanical properties of the model material and rock prototype must be scaled as follows (Ramberg, 1981; Hubbert, 1937):

Eq. 3

$$\frac{C_m}{C_p} = \frac{\rho_m}{\rho_p} \frac{g_m}{g_p} \frac{L_m}{L_p}$$

100 Where C is the cohesion, ρ is the density, g is the gravity acceleration and L is the length.

In some studies (Ramberg, 1967; Harris and Koyi, 2003) the experiments are conducted in an artificial field of gravity, obtained by means of a centrifuge. For experiments performed at normal gravity conditions the ratio $g_m/g_p = 1$ and the eq. 3 can be rewritten as follows:

Eq. 4

105

$$\frac{L_m}{L_p} = \frac{C_m}{C_p} \frac{\rho_p}{\rho_m}$$

The length ratio between the model and prototype (eq. 4) defines the dynamically scaled geometric scaling factor (L*) of the experiment. This relationship represents a critical feature of the model, defining its resolution and, therefore, the structures that can be developed and analysed during the experiment. As a result, the choice of the model material is of primary importance for the physical experiment.

110 Quartz sands, and granular materials in general, are widely used as analogue materials for the physical simulation of brittle upper crust processes (Bonini et al., 2000; Dooley and Schreurs, 2012; Galland et al., 2006; Mcclay et al., 1998), mainly for their handling and mechanical properties. The granular materials can be prepared with many techniques (pouring, sieving, compacting) that determine different values of density and porosity (Panien et al., 2006; Klinkmüller et al., 2016). Also, most of the granular materials can be coloured and different layers can be created in the experiment to improve the

115 visualisation of the developing structures. Finally, the models can be preserved and sliced to analyse the deformation throughout the model.

From the mechanical point of view, granular materials show a complex strain-dependent non-linear deformation behaviour similar to the experimentally deformed natural rocks, with elastic-plastic behaviour, strain hardening and strain softening (Byerlee, 1978; Lohrmann et al., 2003; Mandl, 1988; Marcher and Vermeer, 2001; Panien et al., 2006; Paterson, 1978;

120 Adam et al., 2005).

3. Methods

3.1 Model materials

In this study, the experiments were run with four model materials having the following raw components: quartz sand, clay, and hemihydrate powder. Quartz sand was used as dry sand, preparing the samples with the sieving technique, and as wet

125 sand, prepared by adding 10 wt% of water during the sample preparation. The third analogue material was a mixture of quartz sand with 5 wt% of clay, prepared by sieving. The fourth material was a Granular Rock-Analogue Material (GRAM) composed of quartz sand, hemihydrate powder and water prepared with 2 wt% of hemihydrate powder (Massaro et al., 2022). The chemical compositions of the three basic materials, as defined by the respective suppliers, are summarised in Table 2.

130 Table 2.

The quartz sand is supplied by Minerals Marketing Ltd and is a natural shallow marine sand of the Cretaceous Lower Greensand Fm., extracted from Godstone, Surrey, United Kingdom. The hemihydrate powder is supplied by Scientific Laboratories Supplies and is 100% hemihydrate calcium sulphate powder. The clay bulk mineralogical composition is kaolinite (66%), mica (23%), feldspar (6%), and quartz (1%), supplied by Sibelco UK Ltd.

135 ### 3.1.1 Model material preparation

The four model materials were prepared for mechanical tests and the strike-slip experiments by following a systematic procedure. The sand-clay mixture was prepared by mixing the two components, ensuring that no clay agglomerates formed. The two materials were accurately mixed by using a concrete mixer. Successively, the material was sieved at a constant rate and from a fixed height (about 15 cm) into the mechanical tester cell or the experiment rig. Dry sand did not require any

140 action before sieving it with the same procedure described for sand-clay samples. Wet sand samples were prepared by placing the sand in the concrete mixer, adding 10 wt% of water and mixing to ensure that no dry parts remained. Successively, the material was poured into the mechanical tester cell or experiment rig. GRAM 2% sample preparation was longer since the material requires a stage of drying after the addition of 10 wt% of water to the sand and hemihydrate (2 wt%) mixture (Massaro et al., 2023).

3.1.2 Mechanical properties

The mechanical properties of the sand-clay mixture are investigated by Negrão and Adam (In preparation). The dry quartz sand and GRAM 2% are mechanically characterised in Massaro et al. (2023). The wet quartz sand was mechanically tested in this study. The mechanical test series was performed as described by Massaro et al. (2023), using a specialised dynamic ring-shear tester for powder testing under the range of normal loads observed in analogue modelling (Schulze, 1994; Panien et al., 2006).

The bulk density of the model materials was derived by weighing different samples of known volume and defining the best-fit regression line of the mass/volume graph. Sand-clay 5 wt% mixture shows a density of 1.58 g cm^{-3}, dry sand 1.60 g cm^{-3}, wet sand 1.47 g cm^{-3}, GRAM 2 wt% 1.45 g cm^{-3}.

3.2 Experiment set-up

The physical experiments were run in the Analogue Tectonics Modelling Laboratories of the Department of Earth Sciences at Royal Holloway, University of London (ATML@RHUL). The experiment, also referred to as 'Riedel experiment' (Dooley and Schreurs, 2012), simulates the deformation occurring in an overburden placed on a straight and vertical basement fault (Riedel, 1929). The apparatus is composed of 100 cm-long, 60 cm-wide and 12 cm-high independent metal walls fixed on two mobile metal baseplates (Fig. 1). The baseplates slide against each other along a central straight interface that represents the basement strike-slip fault. All the experiments were run with dextral strike-slip kinematics.

Fig. 1.

The displacement was applied with two different systems depending on the range of material strength. The sand-clay and the dry sand experiments were run with two electric stepper motors, with a constant and pre-defined displacement rate. Each motor pulls one of the baseplates in opposite directions, resulting in a symmetric shear zone. On the other hand, such electronic motors available at the facility are designed for experiments with nearly-cohesionless materials. Therefore, their application for wet sand and GRAM 2% experiments was not possible to avoid damaging the motors themselves. For these experiments, the displacement was applied with a manually driven hydraulic winch. In this way, the displacement rate is not constant and generally higher. Also, only one winch was applied to avoid different displacement rates applied by two operators. Consequently, one of the baseplates is pulled while the other is fixed, forming an asymmetric shear zone.

Additionally, the experiments had individual DIC frame rate values due to the abovementioned differences in the set-up and data acquisition reasons. Therefore, the DIC incremental displacement and strain data are calculated for incremental step size values (i.e., average imposed displacement between two acquired images) individually for each model. The set-up parameters of each experiment are summarised in Table 3.

Table 3.

175 Finally, for all the materials, two independent 1 mm-thick metal baseplates covered with a glued-on rubber sheet were placed on the rig, constituting a high-friction basal interface between the sample and the rig. These rubber sheets were aimed at minimising the slip at the base of the samples.

3.3 DIC analysis

The top surface of the samples was monitored during the experiments. Digital Image Correlation (DIC) techniques were
180 applied to obtain a high-resolution strain monitoring of the models (Adam et al., 2002; Massaro et al., 2022; Adam et al., 2005; Adam et al., 2013; Krezsek, 2007). This analysis technique enables the full-field measurements of the displacement and strain changes, and the monitoring of localised and distributed deformation processes on the model surface. The analysis has a resolution up to the particle scale with a sub-millimetric accuracy (White et al., 2003; Adam et al., 2005). The images were acquired with two high-resolution charge-coupled device (CCD) cameras (Fig. 1). The cameras were fixed
185 symmetrically above the experiment rig in a stereoscopic set-up. Additionally, a third independent camera was fixed above the rig for image acquisition.

The stereo images were sequentially acquired and then processed using Strain Master (LaVision) software, which is a digital image correlation and deformation analysis software adapted for scaled analogue experiments. The 3D experiment surface is calculated from the ortho-corrected stereo images by means of a mathematical mapping function. The latter is derived from
190 3D volume correlation and correction. This procedure is enhanced by a calibration plate with equidistant cross marks on the surface. The calibration plate is placed on the rig during the set-up of the stereo cameras before running the experiment. Additionally, the 3D mapping of the experiment surface is enabled by the volume correlation. Subsequently, the 3D incremental (difference between each image acquired) or total (cumulative values) displacement vector field is calculated by digital image correlation of successive time-series images. Finally, the 3D displacement vector field allows the calculation of
195 additional surface deformation displacement and strain components.

4 Mechanical test results

4.1 Stress-Strain behaviour

The ring-shear test results are shown as shear stress (kPa) and compaction-decompaction (mm) versus shear strain curves (Fig. 2). The four model materials display a non-linear elastic-plastic frictional deformation behaviour with strain hardening
200 and strain softening. In detail, all the samples show the highest values of shear stress during failure of the undeformed material (first peak, τ_{peak}), followed by the second peak (τ_{react}), which is the failure of the second cycle and represents the shear stress needed to reactivate the existing shear zone. On the other hand, the lowest post-failure shear stress values correspond, in all the tested materials, to the stable sliding stages, which define the dynamic-stable strength (τ_{dyn}) necessary for active deformation of the shear zone (fault sliding).

The stress-strain curves regularly vary with different loading conditions, with higher confined stresses requiring higher shear stresses for failure, reactivation, and active slip of shear zones. GRAM 2% displays more irregular trends. At 8 kPa of normal stress, GRAM 2% shows the highest peak strength values (about 13 kPa) and sand-clay the lowest ones (about 6 kPa), whereas wet sand and dry sand have values of about 7 kPa and 6.5 kPa, respectively.

Fig. 2.

The values of compaction (negative dH variations) and decompaction (positive dH variations) occurring within the shear zone, are derived from the vertical displacement of the lid (mm). In all materials, a stage of compaction is observed prior to failure (pre-failure strain hardening). Sand-clay samples display both compaction and decompaction during the test, with higher compaction values observed at higher normal load conditions. In the same way, dry sand samples show less decompaction under higher normal loads and, through the tests, the compaction is observed before the first failure and during the second-cycle stable-sliding phase. Wet sand samples display only compaction throughout the whole duration of the tests, reaching the highest values (-1 mm) of the series. For GRAM samples the compaction-decompaction curves are more irregular with respect to the other analysed materials, although a transition from decompaction to compaction is observed with higher normal loads.

Table 4.

4.2 Cohesion & Frictional Properties

Furthermore, the cohesion, internal friction, and strain hardening/softening parameters were derived from the ring-shear test series (Table 4). The cohesion and internal friction parameters are extrapolated from the critical shear stress/normal stress graphs (Fig. 3) at peak strength, reactivation strength and dynamic-stable sliding. Following the Coulomb failure criterion, the cohesion is the intercept on the y-axis (i.e., the shear strength when the normal stress is zero), while the coefficient of internal friction is derived as the slope of the best-fit regression line. For all the analysed materials the highest values of cohesion are obtained at peak strength, with GRAM 2% and wet sand (7430 and 1428 Pa, respectively) showing values of one order of magnitude higher than dry sand and sand-clay (279 and 189 Pa, respectively).

Fig. 3.

Sand-clay, dry sand, and GRAM 2% show the highest friction coefficients at peak strength (Fig. 4a), whereas for wet sand the highest value corresponds to the reactivation peak friction coefficient (μ_{peak} = 0.6885; μ_{react} = 0.6942). Dry sand and GRAM 2% have similar trends, with a reduction in friction coefficient from peak to reactivation and dynamic-stable strength. Dry sand displays the highest peak friction value (0.77), whereas wet sand has the lowest (0.69).

Fig. 4.

The strain softening is defined as a reduction in strength with equal or increasing strain, determining the weakening of the shear zone. It is quantified as the difference between the peak shear strength and the dynamic-stable strength, divided by the peak shear strength and expressed as a percentage (Panien et al., 2006; Massaro et al., 2023). Sand-clay, wet sand, and GRAM 2% show a decreasing strain softening with higher normal load values, although GRAM 2% displays a much

negative slope coefficient (-1.4×10^{-3}). This trend is similar to what is observed in natural rocks (Ritter et al., 2016). On the other hand, for dry sand samples a positive slope of normal load versus strain softening is observed (Fig. 4b).

240 **4.3 Dynamic scaling**

The model resolution, in terms of geometric scaling factor (L*), derived by the analogue materials in dynamically scaled experiments was calculated following Eq. 4. The experiments were dynamically scaled with respect to a natural prototype to ensure quantitative and qualitative comparison with each other. A generic sedimentary rock was used as a reference natural prototype, with the density, cohesive strength, and coefficient of internal friction described by Kulhawy (1975) and

245 references therein (where they tested several rock formations and provided the average values per rock type).
Fig. 5.

The geometric scaling factors (L*) calculated for the model materials are graphically summarised in Fig. 5. The calculated length equivalences between model (L_m) and prototype (L_p) are 1 cm in the model corresponding to 927 m (sand-clay), 637 m (dry sand), 114 m (wet sand), and 22 m (GRAM 2%). The resolutions obtained with sand-clay mixture and with dry sand

250 allow the simulation at the crustal scale. The wet sand geometric scaling factor falls just above the outcrop scale, corresponding to the field scale. GRAM 2% enables the simulation at the outcrop scale.

5. Experiment results

The strike-slip experiments were systematically performed with the following analogue materials: sand-clay, dry sand, wet sand, and GRAM 2%. In Table 5, the scaling factors are gathered for each of the model materials. The fault displacement

255 rates vary through time (Mouslopoulou et al., 2009) and an average value of 1.45 mm yr^{-1} was used for the scaling calculation.
Table 5.

The experiments were run for a duration and a total horizontal displacement that varied for different model materials, as summarised in Table 3. Sand-clay and dry sand models reached the maximum displacement allowed by the rig (about 15

260 cm), although no more new structures developed on the top surface once the main throughgoing fault was completely connected. The experiments with the manually driven hydraulic winch had a maximum displacement of 10 cm due to asymmetrical set-up constraints. In the wet sand experiments, the maximum displacement was applied, whereas GRAM experiments were stopped at lower values of displacement. This was decided because of the pop-up structures developed in the sample, which with further deformation would have obstructed the surface view of the developing shear zone geometries.

265 In the following section, one representative experiment per material is shown in time-series images of the sample surface at different stages of deformation. We analyse the raw stereo images (image source data) developing a structural map of the digitised fractures, and the different incremental displacement and shear strain components. These include the horizontal shear strain (ε_{xy}), total displacement (d_l), and vertical displacement (d_z) derived from the vector displacement fields.

5.1 Image Source Data

270 The final models presented in Fig. 6 show the different levels of detail provided by the four model materials. The investigation, by moving from sand-clay to dry sand, wet sand and GRAM models, corresponds to a progressive zoom-in into the fault system. The final shear zone is relatively narrower in the sand-clay model, while reaches the highest width in the GRAM model. Consequently, the number of structures developed, and the complexity of the fault system increase with higher model resolutions.

275 Fig. 6.

5.2 Displacement and Strain analysis

The dynamic evolution of the shear zone was quantitatively analysed and compared between the four models at different stages of total horizontal displacement: 2 mm, 4 mm, 6 mm, 8 mm, 10 mm, 20 mm, and 40 mm. The total displacement (d_l, mm), the shear strain ε_{xy} (%) and the vertical displacement (d_z, mm) are shown in Fig. 7, Fig. 8, and Fig. 9, respectively.

280 These displacement and strain data are calculated incrementally between each acquired image, with the frame rates defined in Table 3. The total displacement (d_l) is shown in a scale from 0 to the maximum displacement value (mm) obtained in that frame (Fig. 7). The increments of displacement are regular for sand-clay and dry sand models since the experiments were run with stepper motors. Conversely, wet sand and GRAM incremental displacement values reflect the irregular displacement rates provided by the manually driven hydraulic winch. The shear strain ε_{xy} (expressed in %) is displayed with positive

285 values (warm colours) for dextral shear sense and negative values (cold colours) indicating sinistral shear sense. The vertical displacement (d_z) is shown in mm, with the positive values (warm colours) indicating uplift and the negative values (cold colours) representing subsidence.

Sand-clay model

In the sand-clay model (first column in Fig. 7, Fig. 8, Fig. 9), the first faults are formed in the early stages, with the shear

290 strain clearly localised in a few structures from the 4 mm stage. At 6 mm of displacement, 3-4 *en echelon* fractures form and further develop in the following stages (8-10 mm), increasing in length and broadening the shear zone. In the 20 mm stage, the increase of the shear zone width stops, with the formation of Y shears (horizontal shears) that lead to the complete linkage of the major faults at 40 mm of displacement. In this stage, the displacement and the shear strain are accommodated along the main throughgoing fault. The areas between the main Riedel shears undergo local uplift (from the 8 mm to 20 mm

295 stages), with the maximum values (0.04 mm) of incremental z-displacement observed in the 10 mm stage. The maximum incremental shear strain (0.75 %) is reached in the final examined stage on the main fault.

Dry sand model

In the dry sand experiment (second column in Fig. 7, Fig. 8, Fig. 9), a distributed strain dominates up to the 8-10 mm displacement stages, when the first structures localise. Subsequently, the early shears further develop, temporarily increasing

300 the shear zone width until they completely link together in a narrow primary deformation zone at 40 mm of displacement.

The latter accommodates most of the subsequent displacement. Between 10-20 mm of displacement, the Riedel shears develop increasing in length. Around the 20-40 mm stages, the Y shears form, linking with the early shears and completing the connection within the shear zone. Uplift (positive vertical displacement) is homogeneously distributed in a broad central area of the sample during the first stages (2-10 mm displacement). Successively, it is locally concentrated in specific fault

305   blocks, with the maximum uplift rate (0.17 mm) displayed during the 10 mm stage. Additionally, in the final examined step some subsidence is observed (- 0.05 mm). The maximum shear strain is reached in the final analysed stage (1.30 %) along the main throughgoing fault.

Wet sand model

In the wet sand experiment (third column in Fig. 7, Fig. 8, Fig. 9), the stress localisation starts in the 6 mm stage, when small

310   Riedel shears form in the central part of the sample. Successively, the secondary faults increase in length, broadening the shear zone up to the 20 mm displacement step. During the latter, the shear zone width is at its maximum and the early Y shears develop at lower angles. A few (2-3) secondary P shears are observed in the final stages of deformation, developing between the major faults. The latter, in the next stage, are completely linked together in a throughgoing fault that accommodates most of the successive displacement. The z-displacement progressively localises through the different stages

315   (from the 2 mm displacement), reaching the maximum value (0.12 mm) in the 8 mm stage. Two small areas between the major faults show major uplifts in the 20- and 40-mm stages. In the 40 mm stage, the shear strain reaches its highest value (0.33 %), displayed by the major fully interconnected fault.

GRAM model

The GRAM experiment (fourth column in Fig. 7, Fig. 8, Fig. 9) shows an early compartmentalisation of the displacement in

320   smaller areas defined by early R shears. The strain is localised in 2 main faults in the 4 mm stage. The R shears form in the 2 mm stage and quickly increase in length in the next stage. During the 6 mm step, more secondary R shears and two high-angle shears form. The latter high-angle shears provide linkage between the two early Riedel shears that result completely connected from the 8 mm stage. The shear zone reaches its maximum width at 6 mm of displacement, becoming progressively more complex with the formation of more R, P and Y shears. During the 6-, 8- and 10-mm stages, an antithetic

325   R' shear (sinistral sense of shear) develops between two main R shears. The highest percentage of dextral shear is observed in the final stage (0.60 %) and is displayed by different structures. The highest sinistral shear (0.42 %) is shown in the 10 mm step. The z-displacement is localised in the early stages between the main faults, defining 3-4 areas of local uplift. In the final stages (10-40 mm), the vertical displacement is constant, with an average maximum value of 0.12 mm.

Fig. 7.

330   Fig. 8.

Fig. 9.

In addition to the incremental values, the cumulative displacement and strain parameters were analysed from DIC data. The total shear strain achieved in the final examined stages was compared (Fig. 10). The maximum values of shear strain ε_{xy} (%) observed throughout the experiment surface gradually increase with higher model resolution, with the lowest shear strain

335 reached in the sand-clay model (42%) and the highest in the GRAM model (112%). Similarly, the linearity of the final throughgoing primary deformation zone decreases with higher geometrical resolution of the model, with wet sand and GRAM models developing very complex final shear zones.

Fig. 10.

5.3 Quantitative comparison between the models

340 The DIC strain monitoring of the experiments allowed the quantitative comparison of the displacement and geological strain evolution between the four models. The incremental values (Fig. 11a, b, c) were quantified from Fig. 7, Fig. 8, Fig. 9, from 0 to 40 mm of displacement. The values were normalised to one incremental step size value (in this case we used the sand-clay experiment 0.210 mm step size value, Table 3) to ensure proper comparison between the models. Sand-clay and dry sand models follow similar trends and with comparable values, while wet sand and GRAM models, above all, develop larger

345 values, especially in terms of incremental shear strain.

The total shear strain (Fig. 11d) and total z-displacement (Fig. 11e) were quantified and analysed as the maximum cumulative values recorded at each displacement stage. In the GRAM experiment, the shear strain strongly increases up to more than 100% ε_{xy} in the early stages of deformation but shows only a minor additional increase to nearly 120% ε_{xy} at the experiment completion. Dry sand and wet sand experiments display a similar evolution of cumulative shear strain. GRAM

350 model shows the highest values of total shear strain (about 120% at 60 mm of displacement), followed by wet sand, dry sand, and sand-clay. The sand-clay experiment reached a nearly constant maximum shear strain already between 30 – 40 cm of displacement. The cumulative z-displacement (Fig. 11e) shows a wide range of values between the four models. Overall, the negative z-displacement values (subsidence) are negligible. In detail, the GRAM model reaches the highest uplift values (35 mm), followed by wet sand (14 mm), dry sand (10 mm), and sand-clay (4 mm).

355 The evolution of the shear zone width was analysed at the different stages of displacement (Fig. 11f), quantifying the maximum width of the primary deformation zone and the width of the active shear zone at each individual stage. The evolution of the models from the formation of the early shears to the final interconnected primary fault zone is highlighted. GRAM develops the widest shear zone (~228 mm), followed by wet sand (~195 mm), dry sand (~180 mm) and sand-clay (~131 mm). In terms of active structures, in all the models the maximum shear zone width corresponds to the stage of peak

360 extension of the early R shears. Once the main shear zones are fully interconnected, the deformation is localised in a few major structures and the active shear zone width reduces. This is observed especially in the sand-clay and dry sand models.

Furthermore, the number of active and total structures (i.e., fractures, shears) formed on the samples surface were analysed (Fig. 11g). GRAM developed the most complex shear zone, with the highest number of distinct structures formed during the experiment, followed by wet sand, sand-clay, and dry sand. The number of structures active at the same time has a similar

365 trend for the four models. GRAM final model developed nearly 40 individual structures, with a maximum of about 15

structures active at the same time. On the other hand, the dry sand model developed the lowest number of structures in the final model (12).

Finally, the angles at which the fractures formed with respect to the imposed direction of displacement (σ_1) were measured on the sample surface at the moment they formed (Fig. 11h). According to the Coulomb criterion, the orientations of the
370 potential fault planes in a perfect homogeneous and isotropic material make an angle of $\pm$ 45°−φ/2 to the direction of the maximum principal stress (σ_1). In general, the GRAM model developed structures at higher angles with respect to the other models, including the early R shears and some high-angle synthetic shears. Sand-clay and dry sand models display the lowest angles, on average.

Fig. 11.

375 **6.   Discussion**

The differences between the four models were observed both in the final shear zones (Fig. 6) and during the different stages of deformation (Fig. 7, Fig. 8, Fig. 9). In general, the evolution of the shear zone followed similar key steps in all the models, while showing different kinematics and dynamics detail. The individual shears form in the central part of the shear zone and then develop in length with increasing displacement, eventually linking together in a fully interconnected shear zone. The
380 level of structural detail is different between the four models and has a critical impact on what can be observed and measured during the kinematic and dynamic evolution of the deformation. With lower geometric scaling (i.e., from sand-clay to GRAM models), and therefore higher spatial resolution, the observation of more complex processes within the primary deformation zone is enabled. Although the fault and fracture systems display self-similar scale invariant geometries (Barton and Larsen, 1985; Barton and Zoback, 1992), the multi-scale investigation could improve the understanding of the kinematic
385 and dynamic aspects of such complex deformation processes.

Beyond the complexity of the shear zone developed in the four models, the other main differences observed were the distribution and localisation of the strain and the formation of the pop-up structures.

6.1 Strain localisation

The strain localisation occurs in the early stages of displacement for wet sand and GRAM experiments (Fig. 7, Fig. 8, Fig.
390 9), with the formation of several R shears. On the other hand, in the sand-clay and the dry sand models the deformation is distributed in a wide and continuous shear zone with no distinct structures developed in the first stages of displacement (Fig. 7, Fig. 8, Fig. 9). However, in the sand-clay model, the strain is localised earlier with respect to the dry sand model.

Additionally, the cumulative shear strain patterns enabled the identification of the high-strain structures formed during the experiment (Fig. 10). These show that in sand-clay, dry sand and wet sand models, the early faults that accommodated most
395 of the shear strain are successively inactivated by the complete interconnection of the shear zone. At this point, most of the shear strain takes place along the main throughgoing linked fault zone. The latter develops at a lower angle with respect to

the early R shears and is nearly parallel to the direction of the imposed displacement (σ_1). On the other hand, this is less observed in the GRAM models, where the strain is distributed to various interconnected faults that accommodate most of the following displacement until the end of the experiment (Fig. 10). This is also reflected by the active shear zone width (Fig. 11f) and number of active structures (Fig. 11g) in the final stages. The maximum number of active fractures has been observed at 10-20 mm of displacement, which corresponds to the formation of the main R shears preceding the progressive linkage of the main faults. The latter stage concentrates the shear zone activity in a few major faults in all the models, except for GRAM.

Furthermore, the active shear zone widths displayed in the models confirm that the dry sand model shows the greatest total/active width reduction and the GRAM model the lowest. This suggests that the activity of the final (fully interconnected) shear zone is limited within 24% of the total developed width for the dry sand model, 34% for wet sand, 37% for sand-clay, and 70% for GRAM.

This can be explained by the different levels of detail provided by the models with higher resolution, but also in part by the fact that the experiments performed with wet sand and GRAM undergo an imposed displacement that is not sufficient to complete the evolution of the shear zone, due to the limitations of the rig settings. Wet sand and GRAM experiment, if run for higher displacement values, would most probably reach the same conditions observed in the sand-clay and dry sand models, with full interconnection of the shear zone and concentration of the displacement on one main throughgoing fault. Therefore, this aspect should be further investigated in the future.

6.2 Uplift and pop-up structures

In the GRAM experiment, several pop-up structures developed in the early stages of displacement and increased in dimension until the end of the experiment. This trend is reflected in the incremental and cumulative z-displacement evolution observed during the experiments (Fig. 11c, e). This aspect represents a partial limit of the GRAM experiment set-up that determines a forced earlier termination of the experiments to preserve the developed structures (Massaro et al., 2022). The values of vertical displacement exhibited by the materials clearly depend on the materials cohesive strength. Therefore, this reflects the tendency of high-cohesion materials to form rigid pop-up structures, which are continuously uplifted due to the 3D curved geometries of the helicoidal shape of the strike-slip faults. Overall, in all the models the negative z-displacement (subsidence) is rarely observed. In some cases, low negative values are displayed, corresponding to small collapses of the structures that became unstable because of the uplift in the final stages of displacement.

7. Conclusions

In this study, strike-slip experiments were systematically performed with four different model materials. The comparison between the models was aimed at highlighting the impact of the material mechanical properties on the physical simulation. The four model materials (sand-clay, dry sand, wet sand, and GRAM) were characterised by different physical and

mechanical properties while showing a non-linear strain-dependent behaviour similar to brittle rocks and providing different dynamically scaled geometric scaling factors (in terms of model/prototype length equivalence).

430   Although fault and fracture systems are characterised by a self-similar distribution across the scales, the multi-scale comparison between the models enabled the observation of different kinematic and dynamic characteristics of the developed strike-slip shear zones. From the larger scale to the smaller scale models, the investigation corresponded to a magnification of the shear zone, with increasing complexity of the fault damage zone.

Some of the quantified geometric and kinematic parameters showed a positive relationship with the model resolution. From
435   the largest (sand-clay) to smallest (GRAM) scale, higher values of shear strain, z-displacement, shear zone width, and number of fractures developed were observed. The patterns of strain distribution/localisation displayed higher concentration along fewer structures for the sand-clay and dry sand models, while in the wet sand and GRAM models, the strain was distributed into a more complex network of shears. In all cases, a turning point in the deformation process was represented by the complete interconnection of the primary deformation zone with the development of a main throughgoing fault. The
440   latter tended to concentrate the strain accommodating all the following displacement, especially in the sand-clay and dry sand models.

The multi-scale comparison between the developed models showed how the choice of the analogue material applied in the experiment, its physical and mechanical properties and the consequent scale of observation, critically influence the investigation. Such multi-scale approach can enhance the comprehension of complex brittle deformation processes in
445   dynamically scaled experiments. The application of GRAM in dynamically scaled experiments provides a higher detail on the analysis of the fault-fracture processes occurring within the fault core and fault damage zones.

Data Availability Statement

The data that support the findings of this study are available from the corresponding author upon request.

Author contributions

450   LM, JA, EJ, SN, and YY performed the measurements; LM and JA analysed the data; LM wrote the manuscript draft; LM, JA and YY reviewed and edited the manuscript; JA acquired the funding.

Competing Interest

The authors declare that they have no conflict of interest.

Acknowledgments

455   The work contained in this paper contains work conducted during a PhD study undertaken as part of the Natural Environment Research Council (NERC) Centre for Doctoral Training (CDT) in Oil & Gas (grant number NE/M00578X/1) sponsored by Royal Holloway University of London, whose support is gratefully acknowledged. We extend our thanks to Kevin D'Souza for the photos and for the constructive discussions and to Jerry Morris for the engineering support at RHUL Analogue Tectonic Modelling Laboratories.

460   **References**

Adam, J., Klinkmüller, M., Schreurrs, G., and Wieneke, B.: 4D Simulation of Shear localization and Strain History in Fault systems: Insights from physical experiments, X-ray computed tomography and tomographic digital image correlation, Journal of Structural Geology, 55, 127-149, 10.1016/j.jsg.2013.07.011, 2013.

Adam, J., Lohrmann, J., Hoth, S., Kukowski, N., and Oncken, O.: Strain variation and partitioning in thrust wedges: High-
465   resolution data from scaled sandbox experiments by 2D-3D PIV analysis, Bollettino di Geofisica teorica ed applicata, 42, 123-126, 2002.

Adam, J., Urai, J. L., Wieneke, B., Oncken, O., Pfeiffer, K., Kukowski, N., Lohrmann, J., Hoth, S., van der Zee, W., and Schmatz, J.: Shear localisation and strain distribution during tectonic faulting—new insights from granular-flow experiments and high-resolution optical image correlation techniques, Journal of Structural Geology, 27, 283-301,
470   10.1016/j.jsg.2004.08.008, 2005.

Barton, C. A. and Zoback, M. D.: Self-similar distribution and properties of macroscopic fractures at depth in crystalline rock in the Cajon Pass Scientific Drill Hole, Journal of Geophysical Research: Solid Earth, 97, 5181-5200, https://doi.org/10.1029/91JB01674, 1992.

Barton, C. C. and Larsen, E.: Fractal geometry of two-dimensional fracture networks at Yucca Mountain, southwestern
475   Nevada: proceedings, in: Report Number: CONF-8509129-3, United States, 1985-12-31,   Conference: International symposium on fundamentals of rock joints, Bjorkliden, Lapland (Sweden), 15-20 Sep 1985; Other Information: PBD: 1985,

Billi, A., Salvini, F., and Storti, F.: The damage zone-fault core transition in carbonate rocks: implications for fault growth, structure and permeability, Journal of Structural Geology, 25, 1779-1794, https://doi.org/10.1016/S0191-8141(03)00037-3, 2003.

480   Bisdom, K., Gauthier, B. D. M., Bertotti, G., and Hardebol, N. J.: Calibrating discrete fracture-network models with a carbonate three-dimensional outcrop fracture network: Implications for naturally fractured reservoir modeling, AAPG Bulletin, 98, 1351-1376, 10.1306/02031413060, 2014.

Bonini, L., Sokoutis, D., Mulugeta, G., and Katrivanos, E.: Modelling hanging wall accommodation above rigid thrust ramps, Journal of Struc. Geol., 22, 2000.

485   Byerlee, J.: Friction of rocks, Pure and Applied Geophysics, 116, 615–626, 1978.

Cacciari, P. P. and Futai, M. M.: Modeling a Shallow Rock Tunnel Using Terrestrial Laser Scanning and Discrete Fracture Networks, Rock Mechanics and Rock Engineering, 50, 1217-1242, 10.1007/s00603-017-1166-6, 2017.

Caniven, Y., Dominguez, S., Soliva, R., Cattin, R., Peyret, M., Marchandon, M., Romano, C., and Strak, V.: A new multilayered visco-elasto-plastic experimental model to study strike-slip fault seismic cycle, Tectonics, 34, 232-264,
490   https://doi.org/10.1002/2014TC003701, 2015.

Casas, A. M., Gapais, D., Nalpas, T., Besnard, K., and Román-Berdiel, T.: Analogue models of transpressive systems, Journal of Structural Geology, 23, 733-743, https://doi.org/10.1016/S0191-8141(00)00153-X, 2001.

Childs, C., Nicol, A., Walsh, J. J., and Watterson, J.: Growth of vertically segmented normal faults, Journal of Structural Geology, 18, 1389-1397, http://dx.doi.org/10.1016/S0191-8141(96)00060-0, 1996.

495   Choi, J.-H., Edwards, P., Ko, K., and Kim, Y.-S.: Definition and classification of fault damage zones: A review and a new methodological approach, Earth-Science Reviews, 152, 70-87, https://doi.org/10.1016/j.earscirev.2015.11.006, 2016.

Corti, G., Moratti, G., and Sani, F.: Relations between surface faulting and granite intrusions in analogue models of strike-slip deformation, Journal of Structural Geology, 27, 1547-1562, https://doi.org/10.1016/j.jsg.2005.05.011, 2005.

500 Corti, G., Nencini, R., and Skyttä, P.: Modelling the influence of pre-existing brittle fabrics on the development and architecture pull-apart basins, Journal of Structural Geology, 131, 103937, https://doi.org/10.1016/j.jsg.2019.103937, 2020.

Crider, J. G. and Peacock, D. C. P.: Initiation of brittle faults in the upper crust: a review of field observations, Journal of Structural Geology, 26, 691-707, 10.1016/j.jsg.2003.07.007, 2004.

Dooley, T. and McClay, K.: Analog Modeling of Pull-Apart Basins1, AAPG Bulletin, 81, 1804-1826, 10.1306/3B05C636-172A-11D7-8645000102C1865D, 1997.

505 Dooley, T. P. and Schreurs, G.: Analogue modelling of intraplate strike-slip tectonics: A review and new experimental results, Tectonophysics, 574-575, 1-71, 10.1016/j.tecto.2012.05.030, 2012.

Faulkner, D. R., Jackson, C. A. L., Lunn, R. J., Schlische, R. W., Shipton, Z. K., Wibberley, C. A. J., and Withjack, M. O.: A review of recent developments concerning the structure, mechanics and fluid flow properties of fault zones, Journal of Structural Geology, 32, 1557-1575, https://doi.org/10.1016/j.jsg.2010.06.009, 2010.

510 Fedorik, J., Zwaan, F., Schreurs, G., Toscani, G., Bonini, L., and Seno, S.: The interaction between strike-slip dominated fault zones and thrust belt structures: Insights from 4D analogue models, Journal of Structural Geology, 122, 89-105, https://doi.org/10.1016/j.jsg.2019.02.010, 2019.

Galland, O., Cobbold, P. R., Hallot, E., de Bremond d'Ars, J., and Delavaud, G.: Use of vegetable oil and silica powder for scale modelling of magmatic intrusion in a deforming brittle crust, Earth and Planetary Science Letters, 243, 786-804, 515 10.1016/j.epsl.2006.01.014, 2006.

González, D., Pinto, L., Peña, M., and Arriagada, C.: 3D deformation in strike-slip systems: Analogue modelling and numerical restoration, Andean geology, 39, 295-316, 2012.

Handin, J.: Handbook of Physical Constants, Geological Society of America Memoirs, 97, 223-290, doi: 10.1130/MEM97-p223, 1966.

520 Harris, L. B. and Koyi, H. A.: Centrifuge modeling of folding in high-grade rocks during rifting, Journal of Structural Geology, 25, 291-305, 2003.

Hatem, A. E., Cooke, M. L., and Toeneboehn, K.: Strain localization and evolving kinematic efficiency of initiating strike-slip faults within wet kaolin experiments, Journal of Structural Geology, 101, 96-108, 10.1016/j.jsg.2017.06.011, 2017.

Hubbert, M. K.: Theory of scale models as applied to the study of geologic structures, Geological Society of America 525 Bulletin, 48, 1459-1519, 1937.

Jaeger, J. C., Cook, N. G. W., and Zimmerman, R.: Fundamentals of Rock Mechanics, 4th Edition, Wiley-Blackwell2007.

Kim, Y.-S., Peacock, D. C. P., and Sanderson, D. J.: Fault damage zones, Journal of Structural Geology, 26, 503-517, https://doi.org/10.1016/j.jsg.2003.08.002, 2004.

Klinkmüller, M., Schreurs, G., Rosenau, M., and Kemnitz, H.: Properties of granular analogue model materials: A 530 community wide survey, Tectonophysics, 684, 23-38, https://doi.org/10.1016/j.tecto.2016.01.017, 2016.

Krezsek, C. A., J. and Grujic, D.: Mechanics of fault and expulsion rollover systems developed on passive margins detached on salt; insights from analogue modelling and optical strain monitoring, Geological Society Special Publications, 292, 103-121, 2007.

Krstekanić, N., Willingshofer, E., Broerse, T., Matenco, L., Toljić, M., and Stojadinovic, U.: Analogue modelling of strain 535 partitioning along a curved strike-slip fault system during backarc-convex orocline formation: Implications for the Cerna-Timok fault system of the Carpatho-Balkanides, Journal of Structural Geology, 149, 104386, https://doi.org/10.1016/j.jsg.2021.104386, 2021.

Kulhawy, F. H.: Stress deformation properties of rock and rock discontinuities, Engineering Geology, 9, 327-350, https://doi.org/10.1016/0013-7952(75)90014-9, 1975.

540 Lambert, C., Thoeni, K., Giacomini, A., Casagrande, D., and Sloan, S.: Rockfall Hazard Analysis From Discrete Fracture Network Modelling with Finite Persistence Discontinuities, Rock Mechanics and Rock Engineering, 45, 871-884, 10.1007/s00603-012-0250-1, 2012.

Lohrmann, J., Kukowski, N., Adam, J., and Oncken, O.: The impact of analogue material properties on the geometry, kinematics, and dynamics of convergent sand wedges, Journal of Structural Geology, 25, 1691-1711, 2003.

545 Mammoliti, E., Pepi, A., Fronzi, D., Morelli, S., Volatili, T., Tazioli, A., and Francioni, M.: 3D Discrete Fracture Network Modelling from UAV Imagery Coupled with Tracer Tests to Assess Fracture Conductivity in an Unstable Rock Slope: Implications for Rockfall Phenomena, 10.3390/rs15051222, 2023.

Mandl, G.: Mechanics of tectonic faulting: Models and basic concepts, Developments in structural geology, Elsevier, New York, 407 pp.1988.

550 Marcher, T. and Vermeer, P. A.: Macromodelling of softening in non-cohesive soils, in: Continuous and Discontinuous Modelling of Cohesive-Frictional Materials, edited by: Vermeer, P. A., Herrmann, H. J., Luding, S., Ehlers, W., Diebels, S., and Ramm, E., Springer Berlin Heidelberg, Berlin, Heidelberg, 89-110, 10.1007/3-540-44424-6_7, 2001.

Massaro, L., Adam, J., and Yamada, Y.: Mechanical characterisation of new Sand-Hemihydrate rock-analogue material: Implications for modelling of brittle crust processes, Tectonophysics, 855, 229828, 555 https://doi.org/10.1016/j.tecto.2023.229828, 2023.

Massaro, L., Adam, J., Jonade, E., and Yamada, Y.: New granular rock-analogue materials for simulation of multi-scale fault and fracture processes, Geological Magazine, 159, 2036-2059, 10.1017/S0016756821001321, 2022.

Massaro, L., Corradetti, A., Tramparulo, F. d. A., Vitale, S., Prinzi, E. P., Iannace, A., Parente, M., Invernizzi, C., Morsalnejad, D., and Mazzoli, S.: Discrete Fracture Network Modelling in Triassic–Jurassic Carbonates of NW Lurestan, 560 Zagros Fold-and-Thrust Belt, Iran, Geosciences, 9, 496, 2019.

McClay, K. and Bonora, M.: Analog Models of Restraining Stepovers in Strike-Slip Fault Systems, AAPG Bulletin, 85, 233-260, 10.1306/8626C7AD-173B-11D7-8645000102C1865D, 2001.

McClay, K. and Dooley, T.: Analogue models of pull-apart basins, Geology, 23, 711-714, 10.1130/0091-7613(1995)023<0711:AMOPAB>2.3.CO;2, 1995.

565 McClay, K. R., Dooley, T., and Lewis, G.: Analog modeling of progradational delta systems, Geology, 26, 771–774, 1998.

Mouslopoulou, V., Walsh, J. J., and Nicol, A.: Fault displacement rates on a range of timescales, Earth and Planetary Science Letters, 278, 186-197, 10.1016/j.epsl.2008.11.031, 2009.

Negrão, S. and Adam, J.: A new cohesive granular rock-analogue material and its impact on fault distribution: Structural and quantitative analysis of fault density and growth in scaled analogue rift experiments, In preparation.

570 Panien, M., Schreurs, G., and Pfiffner, A.: Mechanical behaviour of granular materials used in analogue modelling: insights from grain characterisation, ring-shear tests and analogue experiments, Journal of Structural Geology, 28, 1710-1724, 10.1016/j.jsg.2006.05.004, 2006.

Paterson, M. S.: Experimental Rock Deformation, Springer, New York1978.

Ramberg, H.: Model experimentation of the effect of gravity on tectonic processes, The Geophysical Journal of the Royal 575 Astronomical Society, 14, 307-329, 1967.

Ramberg, H.: Gravity, Deformation and the Earth's Crust, Academic Press, New York1981.

Richard, P., Naylor, M. A., and Koopman, A.: Experimental model of strike-slip tectonics, Petroleum Geosciences, 1, 71-80, 1995.

Riedel, W.: Zur Mechanik geologischer Bruchstrukturen, Zentralbl. f. Mineral., Abt. B, 354-368, 1929.

580 Ritter, M. C., Leever, K., Rosenau, M., and Oncken, O.: Scaling the sandbox-Mechanical (dis) similarities of granular materials and brittle rock, Journal of Geophysical Research: Solid Earth, 121, 6863-6879, 10.1002/2016jb012915, 2016.

Schilirò, L., Massaro, L., Forte, G., Santo, A., and Tommasi, P.: Analysis of Earthquake-Triggered Landslides through an Integrated Unmanned Aerial Vehicle-Based Approach: A Case Study from Central Italy, Remote Sensing, 16, 93, 2024.

Schreurs, G.: Experiments on strike-slip faulting and block rotation, Geology, 22, 567-570, 1994.

585 Schreurs, G.: Fault development and interaction in distributed strike-slip shear zones; an experimental approach, Geological Society Special Publications, 210, 35-52, 2003.

Schreurs, G. and Colletta, B.: Analogue modelling of faulting in zones of continental transpression and transtension, Geological Society, London, Special Publications, 135, 59-79, doi:10.1144/GSL.SP.1998.135.01.05, 1998.

Schulze, D.: A New Ring Shear Tester for Flowability and Time Consolidation Measurements, International Particle 590 Technology Forum, Denver/Colorado, USA, 11-16,

Shipton, Z. K. and Cowie, P. A.: Damage zone and slip-surface evolution over μm to km scales in high-porosity Navajo sandstone, Utah, Journal of Structural Geology, 23, 1825-1844, https://doi.org/10.1016/S0191-8141(01)00035-9, 2001.

Wang, L., Chen, W., Tan, X., Tan, X., Yang, J., Yang, D., and Zhang, X.: Numerical investigation on the stability of deforming fractured rocks using discrete fracture networks: a case study of underground excavation, Bulletin of Engineering
595   Geology and the Environment, 79, 133-151, 10.1007/s10064-019-01536-9, 2020.

White, D. J., Take, W. A., and Bolton, M. D.: Soil deformation measurement using particle image velocimetry (PIV) and photogrammetry., Géotechnique, 53, 619-631, 2003.

Wibberley, C. A. J., Yielding, G., and Di Toro, G.: Recent advances in the understanding of fault zone internal structure: a review, Geological Society, London, Special Publications, 299, 5-33, 10.1144/sp299.2, 2008.

600   Wu, J. E., McClay, K., Whitehouse, P., and Dooley, T.: 4D analogue modelling of transtensional pull-apart basins, Marine and Petroleum Geology, 26, 1608-1623, https://doi.org/10.1016/j.marpetgeo.2008.06.007, 2009.

Xiao, Y., Wu, G., Lei, Y., and Chen, T.: Analogue modeling of through-going process and development pattern of strike-slip fault zone, Petroleum Exploration and Development, 44, 368-376, https://doi.org/10.1016/S1876-3804(17)30043-5, 2017.

Zeng, Q. and Yao, J.: Numerical simulation of fracture network generation in naturally fractured reservoirs, Journal of
605   Natural Gas Science and Engineering, 30, 430-443, https://doi.org/10.1016/j.jngse.2016.02.047, 2016.

Figures

Fig. 1. Experiment set-up with stereoscopic CCD cameras and DIC set-up, with a schematic representation of the strike-slip rig (modified after Massaro et al. (2022).

610

-- ----
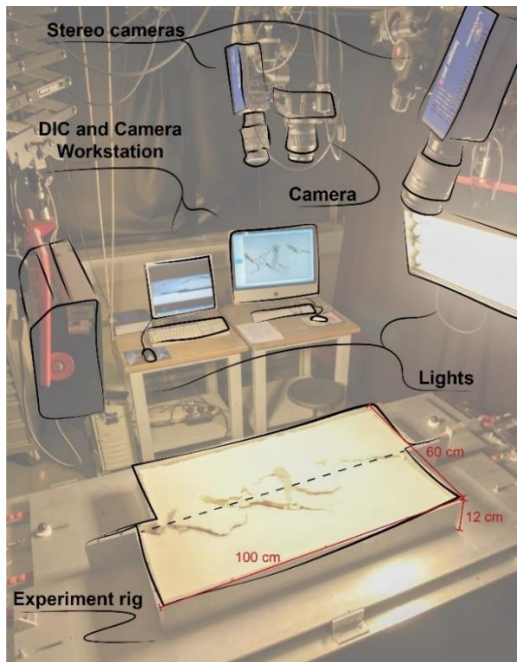
Fig. 2. Shear stress and compaction/decompaction (dH) versus shear strain plots for the analysed materials at different normal load conditions (from 2 to 16 kPa).
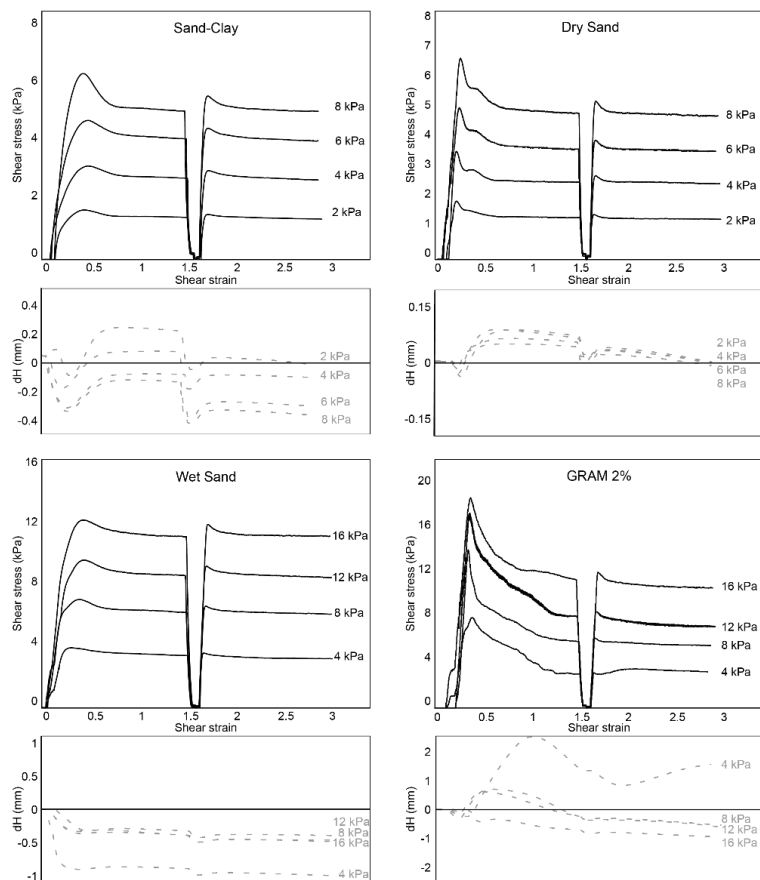
615 --- ----

Fig. 3. Shear stress (kPa) versus normal stress (kPa) graphs for the four analysed materials, with the critical values at peak (black), reactivation (red) and dynamic-stable (blue) strength (modified after Massaro et al. (2023) and Negrão and Adam (In preparation).
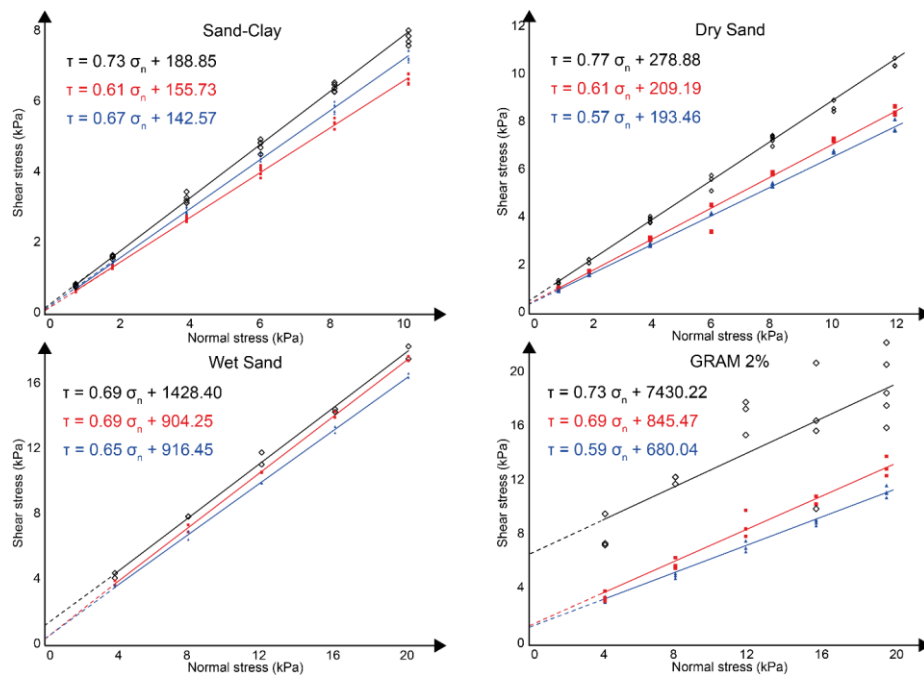
620

Fig. 4. Coefficient of internal friction and strain softening (%) derived from the ring-shear test series for the four analysed materials (modified after Massaro et al. (2023) and Negrão and Adam (In preparation)). a) internal friction coefficients variation at peak strength, reactivation strength and dynamic-stable strength; b) strain softening (%) under different normal load conditions. The equation of the best-fit regression line is reported for each analysed material.
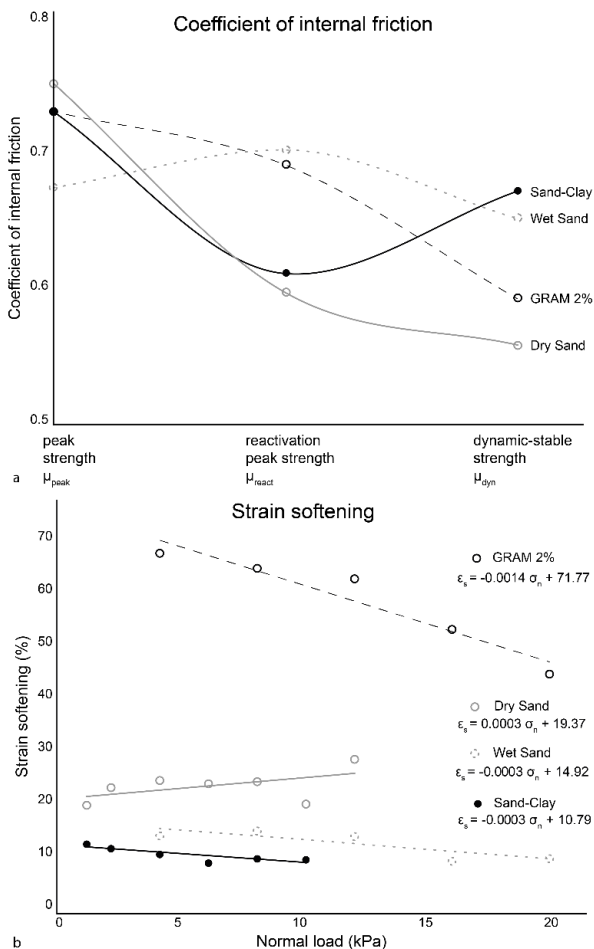
625

-- ----

Fig. 5. Model resolution of the four model materials in terms of dynamically scaled geometric scaling factor (L*) calculated with respect to a sedimentary rock with 2.37 g cm^{-3} of density and 26.3 MPa of cohesion (Kulhawy, 1975).
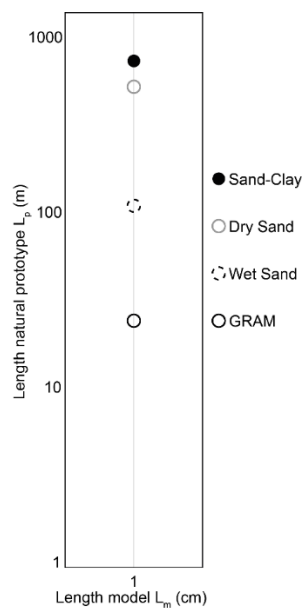
Fig. 6. Comparison of the final models from top-view raw images (image source data) with the structural map of the shear zone geometries. The model-prototype length equivalence (L_m/L_p) and the total displacement (d_l) are reported for each model. The scale in black is related to the model. The scale in red is the corresponding scaled length in the natural prototype.
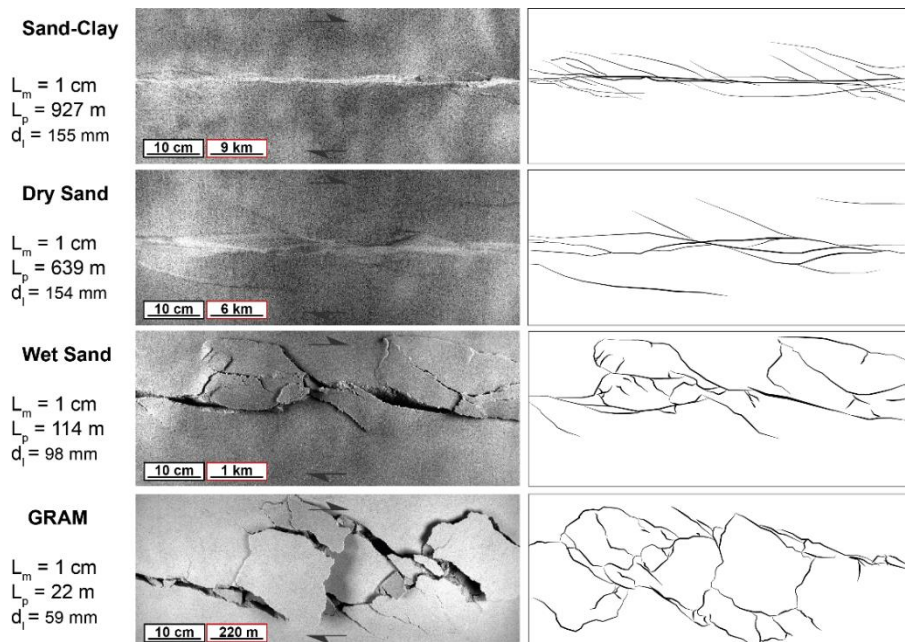
Fig. 7. DIC time-series images of the incremental displacement field (mm) during different stages of the experiments for sand-clay, dry sand, wet sand, and GRAM. The incremental displacement and strain data are calculated for incremental step size values (i.e., average imposed displacement between two acquired images) individually for each model, as shown in Table 3.
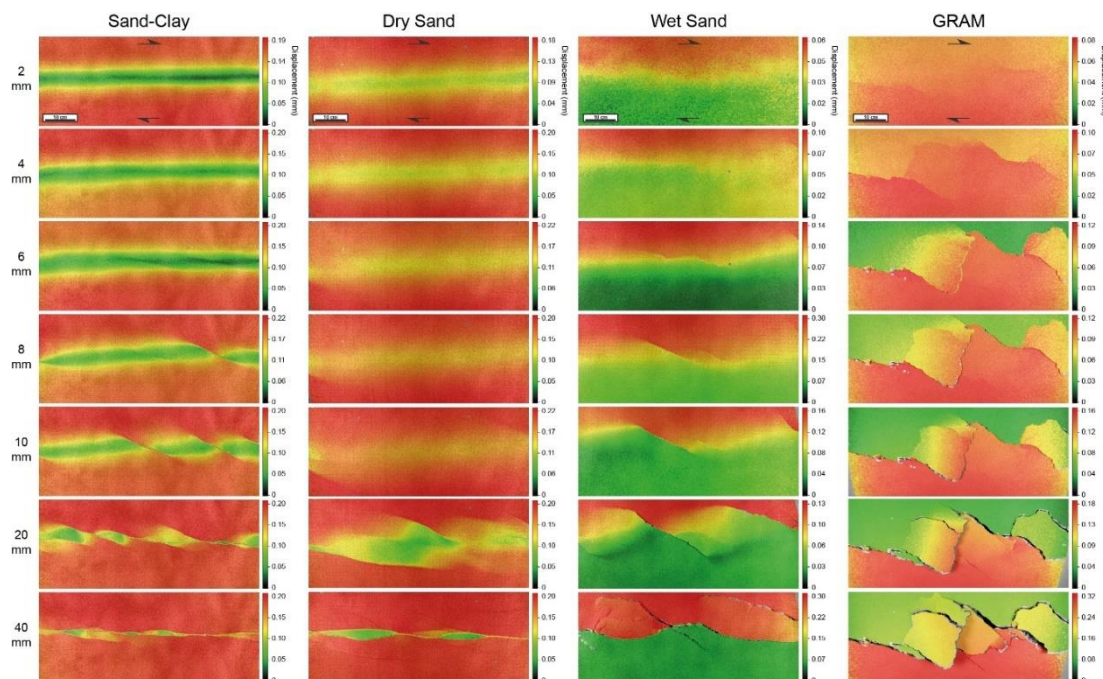
640

-- ----

Fig. 8. DIC time-series images of the incremental shear strain ε_{xy} (%) during different stages of the experiments for sand-clay, dry sand, wet sand, and GRAM. The incremental displacement and strain data are calculated for incremental step size values (i.e., average imposed displacement between two acquired images) individually for each model, as shown in Table 3.
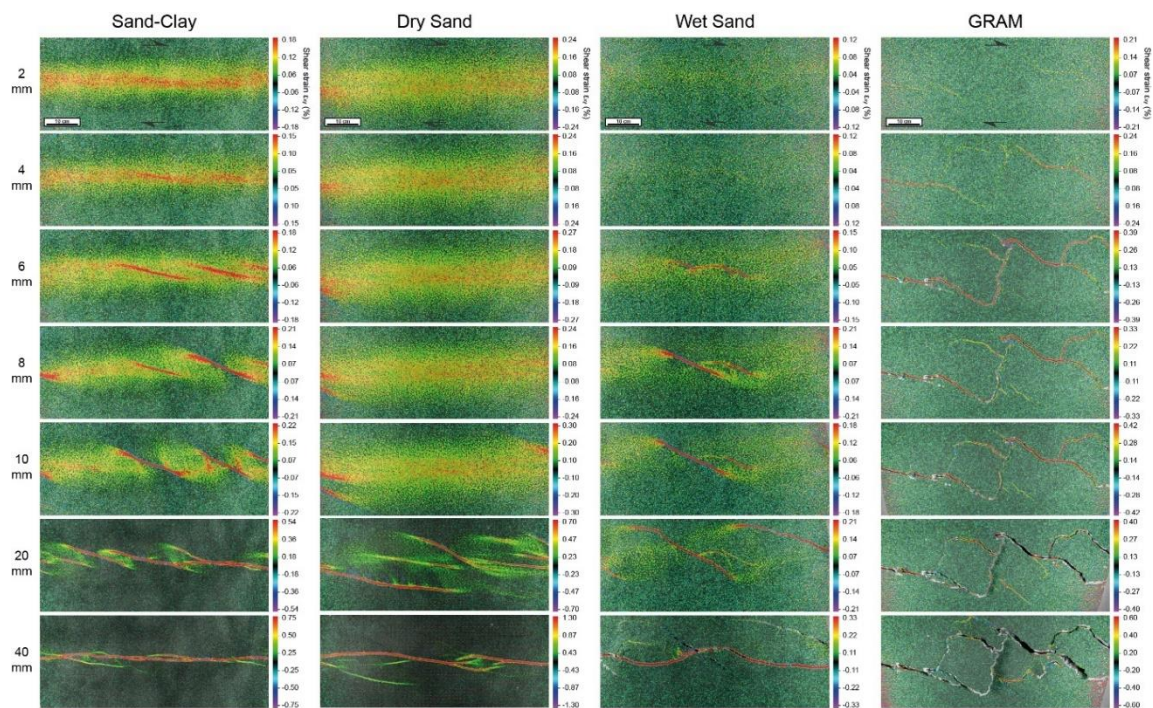
645

Fig. 9. DIC time-series images of the incremental z-displacement field (mm) during different stages of the experiments for sand-clay, dry sand, wet sand, and GRAM. The incremental displacement and strain data are calculated for incremental step size values (i.e., average imposed displacement between two acquired images) individually for each model, as shown in

650   Table 3.
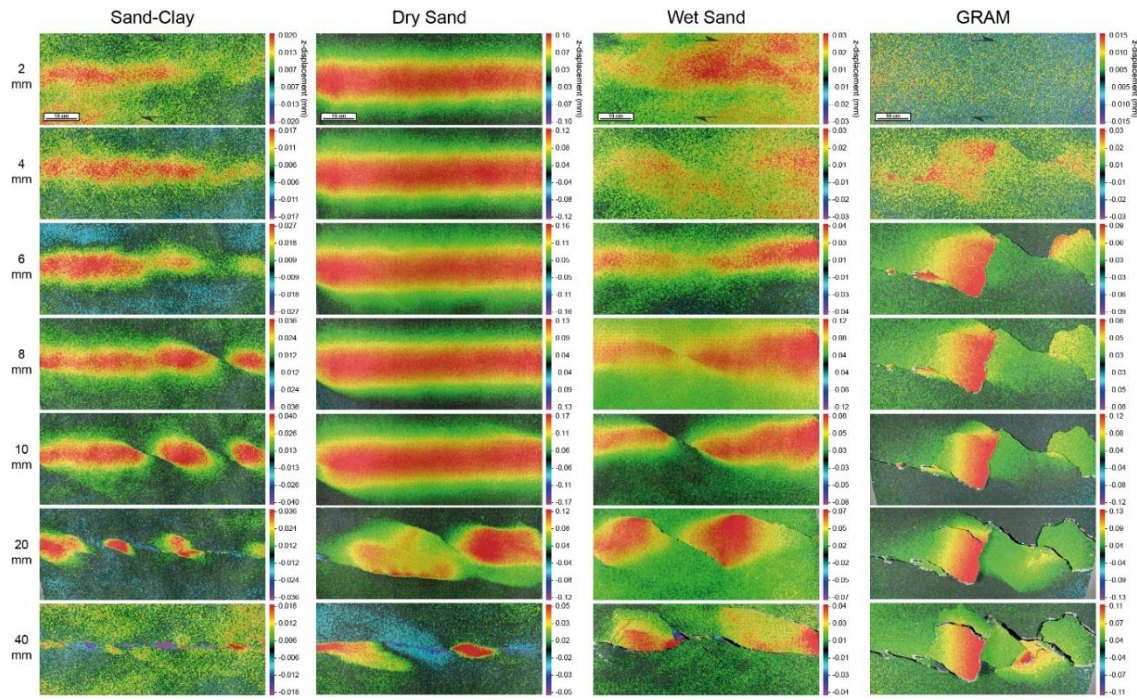
Fig. 10. DIC images of the total shear strain (%) accumulated at the 40 mm displacement stage for the sand-clay, dry sand, wet sand, and GRAM models.
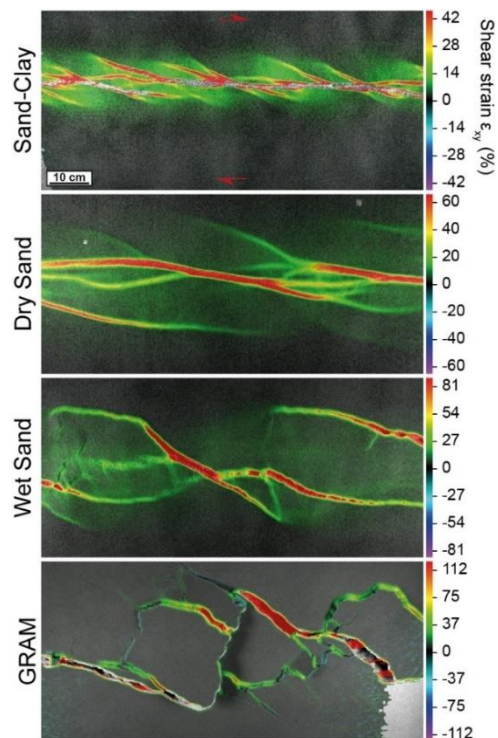
655 --- ----

Fig. 11. Kinematic and dynamic evolution of the sand-clay (black), dry sand (grey), wet sand (blue), and GRAM (red) experiments. a) maximum incremental displacement (mm) versus displacement (mm); b) maximum incremental shear strain (%) versus displacement (mm); c) maximum incremental z-displacement (mm) versus displacement (mm); d) maximum cumulative shear strain (%) versus displacement (mm); e) maximum cumulative z-displacement (mm) versus displacement

660 (mm); f) maximum and active shear zone width (mm) versus displacement (mm); g) cumulative number of structures and active structures developed during the experiment; h) angle of the shears (absolute values) with respect to the direction of the imposed displacement. (φ is the angle of internal friction of each material).
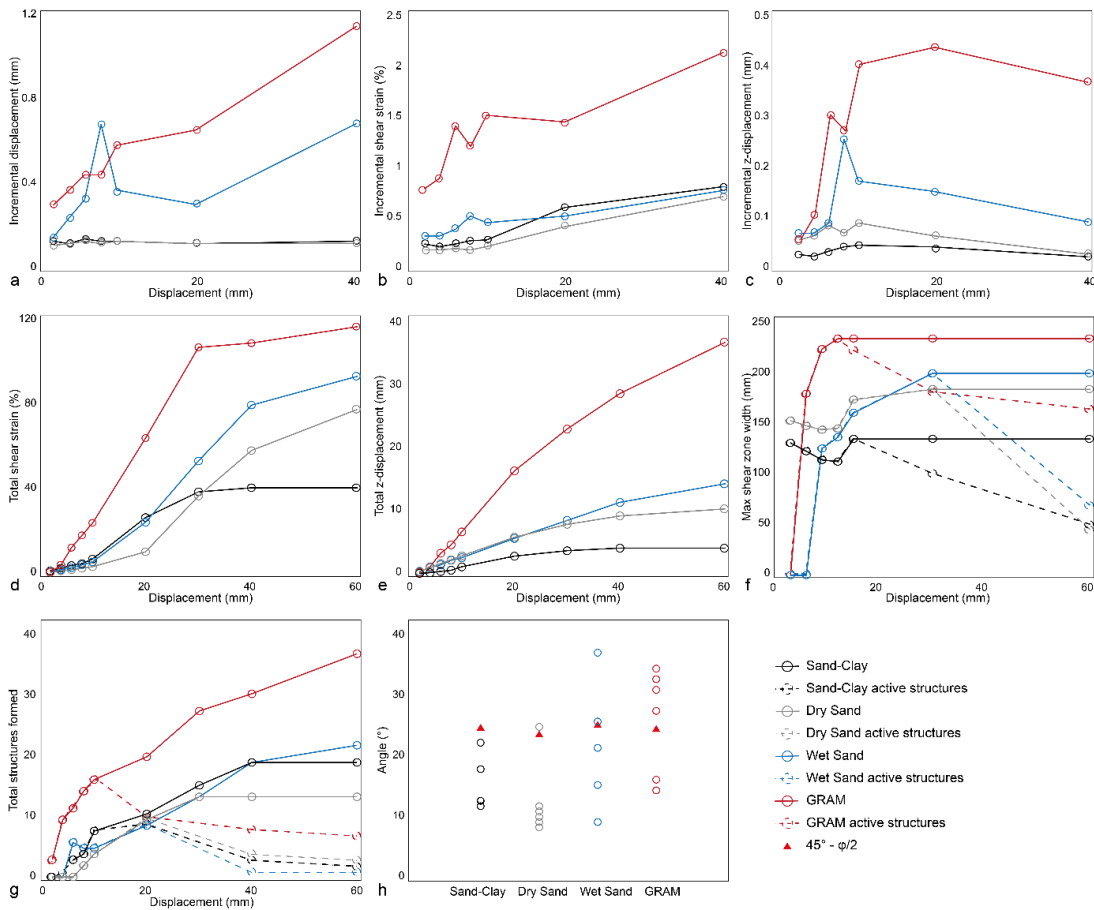
665 **Tables**

Table 1. Summary of the studies on analogue modelling of strike-slip tectonics. PDMS: polydimethylsiloxane silicone.

Study	Scaled length to 1 cm in the model	Analogue materials	Specific focus
Caniven et al. (2015)	2-3 km	Silicone, polyurethane foam, silica powder-graphite mixture	Strike-slip fault seismic cycle
Casas et al. (2001)	1 km	Dry Fontainebleau sand, silicone putty	Transpressive systems
Corti et al. (2005)	10 km	Dry Quartz sand, PDMS, silicone-oleic acid mixture	Emplacement of granitic magmas at upper crustal levels during strike-slip deformation
Corti et al. (2020)	~3 km	Quartz sand, K-feldspar sand, PDMS	Pull-apart basins development and architecture in the presence of inherited discrete brittle fabrics
Dooley and Mcclay (1997)	1 km	Dry quartz sand	Pull-Apart Basins
Dooley and Schreurs (2012)		Quartz sand, wet clay, PDMS, corundum sand, glass powder	Riedel experiment, Transpression and transtension, Oblique-slip, Distributed strike-slip shear experiments, pull-apart basins, restraining stepovers or bends, Effect of crustal weak zones on strike-slip fault-zone segmentation, reactivation of extensional basins, intraplate strike-slip tectonics
Fedorik et al. (2019)	1 km	Dry quartz sand	Strike-slip tectonics interaction with thrust belt structure
González et al. (2012)	1 km	Dry quartz sand	Pure and transpressional-transtensional strike-slip systems
Hatem et al. (2017)	0.5 -1.2 km	Wet kaolin	Strain partitioning in strike-slip fault system
Krstekanić et al. (2021)	7 km	Dry quartz sand, PDMS-iron powder-quartz sand mixture	Strain partitioning in strike-slip fault system
Mcclay and Bonora (2001)	1 km	Dry quartz sand	Pop-up development in restraining stepovers
Mcclay and Dooley (1995)	1 km	Dry quartz sand	Pull-Apart Basins
Richard et al. (1995)	750 m	Dry sand	Strike-slip tectonics
Schreurs (1994)	5 km	Dry quartz sand, glass powder, PDMS	Strike-slip faulting in zones of distributed shear deformation and block rotation
Schreurs (2003)	0.5 – 5 km	Dry quartz sand, glass powder, PDMS	Distributed strike-slip shear zones
Schreurs and Colletta (1998)	0.5-5 km	Dry quartz sand, glass powder, PDMS	Transpressional and transtensional tectonics
Wu et al. (2009)	1 km	Dry quartz sand	Pull-apart basins
Xiao et al. (2017)	1 km	Dry and wet quartz sands	Simple shear strike-slip fault zone

-- ----

Table 2. Chemical composition of the raw materials as provided by the suppliers. LOI: Loss On Ignition.

Quartz Sand		Hemihydrate powder		Clay	
SiO_2	99.70%	$CaSO_4 \cdot \frac{1}{2}H_2O$ 100%		SiO_2	48.30%
Fe_2O_3	0.05%			Al_2O_3	36.28%
Al_2O_3	0.08%			K_2O	2.60%
K_2O	0.01%			Fe_2O_3	0.80%
LOI	0.10%			MgO	0.40%
				Na_2O	0.10%
				CaO	0.06%
				TiO_2	0.04%
				LOI	11.60%

670   Table 3. Specifics of the experiments analysed in this study with sand-clay, dry sand, wet sand, and GRAM 2%.

Experiment ID	Sand-clay	Dry sand	Wet sand	GRAM 2%
Model materials	Quartz Sand, Clay	Quartz sand	Quartz sand, water	Quartz sand, hemihydrate powder, water
Sample dimension	100 x 60 x 10 cm			
Initial set-up	Horizontal and homogeneous sample			
Rig set-up	Single planar and vertical basement fault			
Kinematic	Dextral strike-slip			
Basal Interface	Metal baseplate with rubber sheet			
Total Displacement	15.5 cm	15.4 cm	9.8 cm	5.9 cm
Displacing system	2 stepper motors	2 stepper motors	Hydraulic winch	Hydraulic winch
Duration	123' 13''	122' 26''	16' 51''	16' 13''
Average displacement rate	1.26 mm min^{-1}	1.26 mm min^{-1}	5.82 mm min^{-1}	3.64 mm min^{-1}
DIC frame rate	0.1 Hz, $\Delta t = 10$ s	0.05 Hz, $\Delta t = 20$ s	1 Hz, $\Delta t = 1$ s	1 Hz, $\Delta t = 1$ s
Incremental step size	0.210 mm	0.420 mm	0.097 mm	0.061 mm
DIC raw data	739 images	367 images	1011 images	973 images

Table 4. Mechanical properties derived from ring-shear test series for sand-clay (Negrão and Adam, In preparation), dry sand (Massaro et al., 2023), wet sand, GRAM 2% (Massaro et al., 2023): angle and coefficient of internal friction and

extrapolated cohesion at peak, reactivation and dynamic-stable strength, and percentage of strain softening/hardening. The

675   error is the standard error calculated after linear regression.

	Angle and coefficient of internal friction			Cohesion			Strain softening at $\sigma_n = 0$
	Peak	Reactivation	Dynamic	Peak	Reactivation	Dynamic	
	μ φ (°)	μ φ (°)	μ φ (°)	C (Pa)	C (Pa)	C (Pa)	
Sand-clay	0.73 ± 1% 36.1	0.61 ± 1% 31.5	0.67 ± 1% 33.9	189 ± 33%	156 ± 20%	143 ± 23%	11%
Dry sand	0.77 ± 1% 37.7	0.61 ± 3% 31.5	0.57 ± 0.5% 29.8	279 ± 21%	209 ± 41%	193 ± 8%	19%
Wet sand	0.69 ± 2% 34.5	0.69 ± 1% 34.8	0.65 ± 1% 33.0	1428 ± 16%	904 ± 12%	916 ± 12%	15%
GRAM 2%	0.73 ± 17% 36.1	0.69 ± 5% 34.6	0.59 ± 2% 30.5	7430 ± 22%	845 ± 49%	680 ± 27%	72%

Table 5. Scaling factors of the four experiments. The natural prototype physical and mechanical properties are referred to a generic sedimentary rock (Kulhawy, 1975) and the displacement rate of the natural system is from Mouslopoulou et al. (2009).

	Natural prototype	Sand-Clay	Dry Sand	Wet sand	GRAM 2%
Internal friction coefficient	0.72	0.73	0.77	0.69	0.73
Scaling factor		~1	~1	~1	~1
Internal friction angle (°)	36	36	38	35	36
Scaling factor		~1	~1	~1	~1
Cohesion (MPa)	26.30	1.89×10^{-4}	2.79×10^{-4}	1.43×10^{-3}	7.43×10^{-3}
Scaling factor		7.19×10^{-6}	1.06×10^{-5}	5.43×10^{-5}	2.83×10^{-4}
Density (g cm^{-3})	2.37	1.58	1.60	1.47	1.45
Scaling factor		0.67	0.68	0.62	0.61
Gravity acceleration	9.81	9.81	9.81	9.81	9.81
Scaling factor		~1	~1	~1	~1
$L^* = \dfrac{L_m}{L_p} = \dfrac{C_m}{C_p}\dfrac{\rho_p}{\rho_m}\dfrac{g_p}{g_m}$		1.08×10^{-5}	1.57×10^{-5}	8.76×10^{-5}	4.63×10^{-4}
L_p (m) (L_m = 1 cm)		927	637	114	22
Displacement rate	1.45 mm yr^{-1}	1.26 mm min^{-1}	1.26 mm min^{-1}	5.82 mm min^{-1}	3.64 mm min^{-1}
Scaling factor		4.56×10^5	4.56×10^5	2.11×10^6	1.32×10^6